



Amplification of nonlinear polariton pulses in waveguides

LUCY E. TAPIA RODRIGUEZ,¹ PAUL M. WALKER,^{1,*}
HELGI SIGURDSSON,² BEN ROYALL,¹ IAN FARRER,³ DAVID A.
RITCHIE,⁴ ALEXEY V. YULIN,⁵ IVAN A. SHELYKH,^{2,5} MAURICE S.
SKOLNICK,^{1,5} AND DMITRY N. KRIZHANOVSKII^{1,5}

¹*Department of Physics and Astronomy, University of Sheffield, S3 7RH Sheffield, UK*

²*Science Institute, University of Iceland, Dunhagi-3, IS-107 Reykjavik, Iceland*

³*Department of Electronic and Electrical Engineering, University of Sheffield, S3 7HQ Sheffield, UK*

⁴*Cavendish Laboratory, University of Cambridge, CB3 0HE Cambridge, UK*

⁵*Department of Nanophotonics and Metamaterials, ITMO University, St. Petersburg 197101, Russia*

**p.m.walker@sheffield.ac.uk*

Abstract: Using a sub-millimeter exciton-polariton waveguide suitable for integrated photonics, we experimentally demonstrate nonlinear modulation of pico-Joule pulses at the same time as amplification sufficient to compensate the system losses. By comparison with a numerical model we explain the observed interplay of gain and nonlinearity as amplification of the interacting polariton field by stimulated scattering from an incoherent continuous-wave reservoir that is depleted by the pulses. This combination of gain and giant ultrafast nonlinearity operating on picosecond pulses has the potential to open up new directions in low-power all-optical information processing and nonlinear photonic simulation of conservative and driven-dissipative systems.

Published by The Optical Society under the terms of the [Creative Commons Attribution 4.0 License](#). Further distribution of this work must maintain attribution to the author(s) and the published article's title, journal citation, and DOI.

1. Introduction

Exciton-polaritons are the quasiparticles formed by strong coupling of photons and quantum-well excitons [1]. They combine photon-like propagation with giant effective $\chi^{(3)}$ nonlinearity arising from interactions between their excitonic components. These properties have led to great interest in using polaritons for applications in photonics [2]. In GaAs Fabry-Perot microcavities devices such as switches [3–6] transistors [7] and diodes [8] have been demonstrated. A promising alternative to microcavities are polariton waveguides [9], where optical confinement is due to total internal reflection. They provide many advantages such as stronger photon-exciton coupling, longer propagation distances and considerably easier growth and fabrication. These aspects make them advantageous for applications in all-optical information processing where propagation speed and bandwidth are important and also for photonic simulation where, because of the high longitudinal wavenumber, the propagation distance along the waveguide plays the role of time [10]. So far several fundamental nonlinear optical phenomena such as bright [11] and dark [12] solitons have been observed in polariton waveguides.

The excitonic component of polaritons also allows for optical amplification schemes [13–15]. Polariton lasers based on parametric scattering (OPO) [16, 17] and final state stimulation [18–21] have been demonstrated. Polariton devices operate at densities below the Mott density at which the exciton oscillator strength is quenched and polaritons no longer exist [22]. This is in contrast to traditional semiconductor optical amplifiers (SOAs) which use a high density inverted carrier population to provide gain through stimulated emission [23, 24]. SOAs provide high gain but their nonlinear response originates from gain saturation [23] and the speed is limited by the gain-recovery time, ultimately linked to carrier lifetime, and is typically more than 10 picoseconds (ps). By contrast the polariton nonlinearity operates on a picosecond timescale, an order of

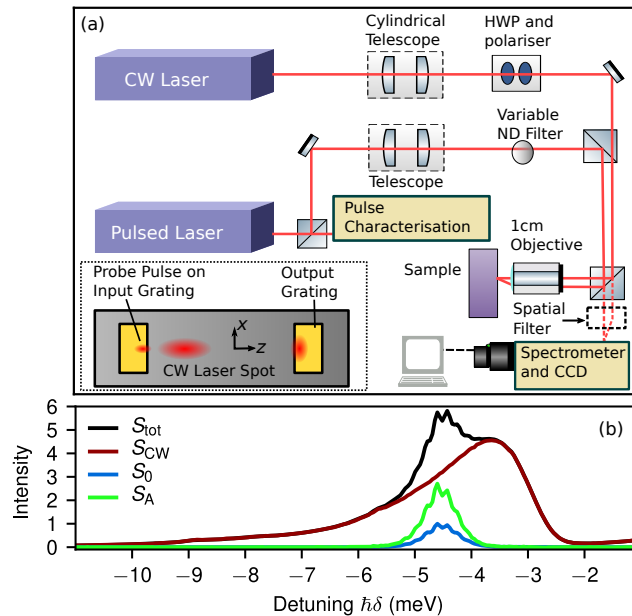


Fig. 1. (a) Schematic of the optical setup for excitation of the sample and detection of the emission. Inset in the bottom left is a top-down schematic of the sample surface showing the low power picosecond pulsed probe laser spot on the input grating coupler and the CW pump spot between the grating couplers. (b) Spectra of the light collected at the output grating for the maximum pump power of 50mW and the minimum probe power corresponding to 72fJ pulses. The horizontal axis gives the frequency offset from that of the exciton, $\delta = \omega - \omega_X$. A detailed description of the legend labelling is given in the text. S_{tot} , S_{CW} and S_0 are the spectra obtained when, respectively, both pump and probe beams are switched on, only the pump beam is switched on, only the probe beam is switched on. S_A is obtained by subtracting S_{CW} from S_{tot} .

magnitude faster [11]. Furthermore, waveguide geometries are particularly advantageous for polariton amplification devices since optical pumping of the exciton states is not spectrally blocked by DBR mirrors, as it is in microcavities. Amplifiers based on ZnO polariton waveguides have been proposed in [25] and demonstrated in the quasi-continuous-wave regime [26]. Amplification of picosecond pulses and the important question of whether nonlinearity can be retained alongside amplification have not previously been studied.

In this work we show that polaritons can simultaneously provide gain sufficient to overcome system losses and strong nonlinear response for pico-Joule pulses and sub-millimeter length scales suitable for integration of devices on a chip. This has potential to open up new directions for small-footprint low-power all-optical information processors where control over and compensation of optical losses is important. Our platform can also allow creation of complex spatially modulated gain and loss profiles opening up new routes towards photonic simulation including of driven-dissipative systems where gain, loss and nonlinearity all acting on short length scales can open up rich new physics [27, 28] compared to conservative systems and can lead to new types of devices such as unidirectional optical valves, all-optical switches, lossless solitons, enhanced sensors [29] and platforms for studying novel extensions to topological physics [30].

2. Experimental methodology

We used a GaAs planar waveguide with 3 InGaAs Quantum Wells embedded in the core (see Appendix C for additional experimental details). Light was injected and collected using a single microscope objective and two diffractive grating couplers patterned on the sample surface and separated by 400 μm . The sample was held at a temperature of ~ 10 Kelvin in a liquid helium cold-finger cryostat. We focused 2 ps laser pulses, hereafter referred to as the *probe* pulses, onto the input grating coupler and collected the light after it had propagated to the output coupler, as shown in Fig. 1(a). The 2ps pulses were generated by a tuneable mode-locked laser at a rate of 80MHz (see Appendix C). The spatial width of the pulsed laser spot in the x direction (transverse to propagation) was 4.3 μm at the input grating. By the output grating this width increases to 11.2 μm due to diffraction in the waveguide. A continuous-wave (CW) laser (hereinafter referred to as the *pump*) at the exciton wavelength (836.9 nm) optically excites a region of the sample between the two gratings. The size of the pumped region was 30 μm in the x direction, much wider than the probe pulse. In the direction of propagation the pumped region was 100 μm long and had its peak 120 μm away from the input grating. The pump was normally incident on the sample and, since there was no grating coupler in its vicinity, it does not directly excite the high momentum (23.6 μm^{-1}) polariton modes outside the light cone (see [11, 12] for waveguide dispersion) but only pumps the exciton states close to zero in-plane momentum. The collected light was spatially filtered in order to detect only the emission from the output grating coupler, over 280 μm away from the pump spot. It was then focussed onto an imaging spectrometer fitted with a CCD camera and resolved in real space and wavelength simultaneously.

For a range of pump powers, and pulse energies and detunings δ_0 from the exciton, the spectrum was recorded in three configurations. These spectra are shown in Fig. 1(b) where S_0 is the spectrum obtained with only the probe pulse excitation switched on, S_{CW} is for only the pump beam switched on and S_{tot} is for both present. The spectrum S_{CW} is generated as follows. The pump resonantly excites exciton states near zero in-plane momentum. These then relax their energy and momentum through multiple exciton and phonon scatterings thus creating an incoherent reservoir of excitons with a range of energies and momenta. A small fraction relax to high momentum polariton states outside the light cone which are able to propagate the ~ 280 μm to the output grating where they are diffracted out and give rise to S_{CW} . The spectrum S_0 is from the pulses transmitted from input to output grating. To obtain the effect of the pump on the probe pulses we subtract S_{CW} from the total emission S_{tot} to obtain the amplified pulse spectrum S_{A} . To obtain the gain factor G we then integrate both S_{A} and S_0 with frequency δ over the same spectral region and divide the former by the latter to obtain the values plotted as points in Fig. 2. We note that these values can be converted to a gain in decibels using the formula $G_{\text{dB}} = 10\log_{10}(G)$. This latter form is useful for comparison with waveguide losses as done in Table 4. The subtraction procedure we have detailed is necessarily sensitive to the signal-to-background ratio between the pulse-only spectrum S_0 and the pump-only spectrum S_{CW} . The case shown in Fig. 1(b) is that for the maximum pump power (50mW CW) and minimum probe pulse power (72 fJ) and is the one for which we obtain the maximum gain of 2.7. It is also the case with the lowest signal-to-background ratio. The ratio is 0.33, as can be seen by comparing the two curves at the energy corresponding to the peak of S_0 . Although the signal is lower than the background this ratio is still sufficient to make useful measurements since the fluctuations in the background signal are only of order 1% (see Appendix B for further discussion of the signal-to-noise and signal-to-background ratios). The fluctuations are accounted for in the error bars shown in Fig. 2. We finally note that although the pulse signal shown here for the case of maximum gain is 3 times lower than the background the pulse duty cycle is only 2 picoseconds in every 12.5 nanoseconds (see Appendix C) so that on the picosecond timescale relevant for applications involving interacting pulses the signal to background ratio is 6250 times better than it appears in this time-averaged measurement.

3. Theoretical model

It can be seen in Fig. 1(b) that S_A has been amplified compared to S_0 . The gain is provided by stimulated scattering from the background reservoir of excitons and polaritons generated by the pump [13, 14, 31]. We model this process using a generalised Gross-Pitaevskii (or Nonlinear Schrodinger) equation describing the coherent field of the lower polariton branch (LPB) (ψ) and a rate equation for the reservoir (n).

$$i\dot{\psi} = \left[\varepsilon - i\frac{\gamma}{2} + \left(g + i\frac{R}{2} \right) n + \alpha|\psi|^2 \right] \psi + F, \quad (1)$$

$$\dot{n} = - \left(\Gamma + R|\psi|^2 \right) n + P. \quad (2)$$

Here, ε is the lower polariton branch (LPB) dispersion, γ and Γ are the polariton and reservoir inverse lifetimes, g and α are the polariton-reservoir and polariton-polariton interaction strengths, R is the reservoir gain, F is the coherent pulse, and P is the nonresonant pump. The LPB dispersion is calculated from the strongly coupled exciton resonance (ε_X) and waveguide photon dispersion (ε_P),

$$\hat{\varepsilon} = \frac{\hat{\varepsilon}_X + \hat{\varepsilon}_P}{2} - \frac{\sqrt{(\hat{\varepsilon}_P - \hat{\varepsilon}_X)^2 + \Omega^2}}{2}, \quad (3)$$

where Ω is the Rabi frequency, which gives the strength of the photon-exciton coupling, and the caret ($\hat{}$) notation denotes reciprocal space operators. We define the exciton-photon resonance as the zero energy and zero wavevector position in reciprocal space. Applying the slowly-varying-envelope approximation to the waveguide photon mode we have $\varepsilon_P = -iv_g\partial_z$ where v_g is the group velocity of the light in the strong coupling regime. The pulse and the pump are written,

$$F = F_0 \exp \left[-i(\omega_p t - k_p z) - t^2/2\sigma_t^2 - z^2/2\sigma_z^2 \right], \quad (4)$$

$$P = P_0 \exp \left[-(z - z_0)^2/2\sigma_{CW}^2 \right]. \quad (5)$$

Details of the parameters used are given in Appendix A. We note that values of the gain coefficient R and reservoir inverse lifetime Γ are obtained as fitting parameters used to match the experiment data.

Numerically integrating (1) and (2) provides the spectrum of the coherent polariton field for given pump power and probe parameters. These spectra may be examined directly (as we do later in Fig. 4) or integrated in the same way as the experimental spectra (see above) to provide the simulated gain factor. The simulated gain vs. pump power and probe parameters are shown as solid lines in Fig. 2. The simulations semi-quantitatively reproduce the main features of the experimental data (shown as points), showing a gain which increases close to linearly with pump power and which decreases as the pulse central frequency is detuned further from the exciton (as $|\delta_0|$ increases).

4. Results and discussion

The points in Fig. 2 shows the integrated experimental S_A intensity normalised to that of S_0 as a function of the pump power for several different pulse parameters. This corresponds to the gain experienced by the probe pulses due to the presence of the pump. The error bars are estimated from the measured shot-to-shot fluctuations in S_{CW} and S_0 . In all cases the gain increases with increasing pump power as expected. While the gain increases with *pump* we also observe that it decreases as the *probe* pulse energy is increased from 72fJ to 7.2pJ from panel (a) to (b) to (c). This points to saturation of the gain due to partial depletion of the reservoir [13, 32]. This is confirmed by the simulations, where the reservoir density n is observed to be depleted as the pulse passes through. For the probe pulses with detuning $\delta_0 = -5.6$ meV and -6.1 meV the gain

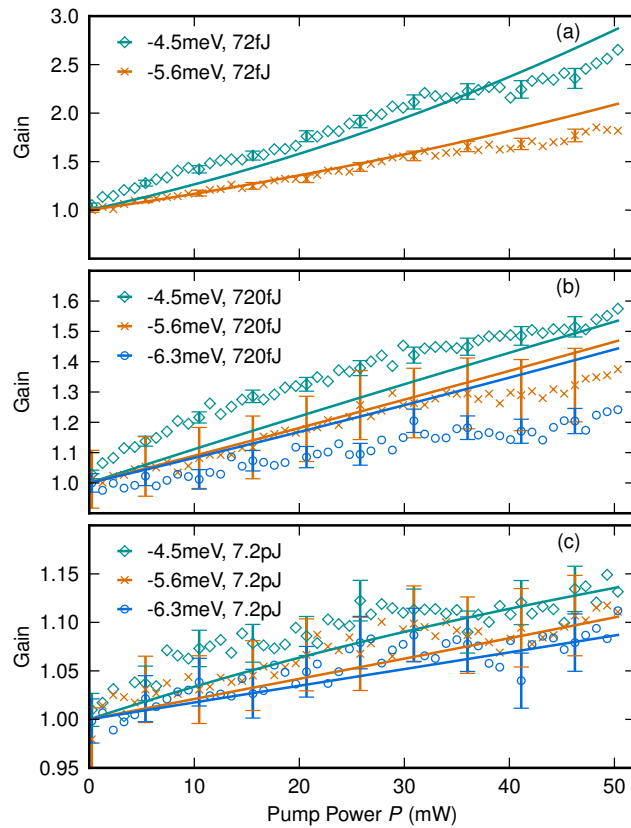


Fig. 2. Gain experienced by the probe pulses as a function of pump power for various probe detunings and pulse energies. Experimental data are shown as points and results of numerical simulations are shown as solid lines. Panels (a), (b), and (c) show data for probe pulse energies of 72fJ, 720fJ and 7.2pJ respectively. For clarity error bars are only shown for every fifth point but are of similar size for all points.

increases close to linearly with pump power. One might expect the gain to increase super-linearly with the pump since the pulse grows exponentially with the stimulated scattering rate [13, 14]. However, the depletion prevents this since the pulse can only grow until it exhausts the reservoir. For the pulses detuned closer to the exciton at $\delta_0 = -4.5$ meV the output vs. input is sub-linear. This sub-linearity is more pronounced for the 720 fJ pulse in panel (b) than for the weaker pulse in panel (a) and, notably, was not present in the simulations. This is likely due to exciton broadening at high pump powers leading to increased absorption for the detuning $\delta_0 = -4.5$ meV. We note that at low density strong absorption begins close to this value at -3.8 meV [12].

Table 4 gives the maximum gain for various probe parameters as well as the linear loss over the $100 \mu\text{m}$ length corresponding to the pump spot [12]. It can be seen that for the 72fJ and 720fJ pulses the gain is sufficient to overcome the loss in the pumped region. We note that the total length of the device is $400 \mu\text{m}$ so that $300 \mu\text{m}$ of the device is unpumped and therefore experiences a net loss. For the 7.2pJ pulses the gain is still present but only partially compensates the loss in the pumped region. We note that additional loss is present at this pulse power because, as we will discuss next, the nonlinear processes scatter polaritons into a high absorption spectral region close to the exciton line. This nonlinear loss contribution reduces the apparent gain we measure.

Table 1. Gain at the maximum pump power for all the different probe parameters^a.

	-4.5meV	-5.6meV	-6.3meV
Max. Gain (dB) (72fJ)	4.3	2.7	-
Max. Gain (dB) (720fJ)	1.96	1.37	0.93
Max. Gain (dB) (7.2pJ)	0.57	0.45	0.37
Loss over 100 μm (dB)	0.97	0.90	0.86

^a For comparison the linear loss over 100 μm , corresponding to the pump spot length, is given on the last row (data taken from data in [12]).

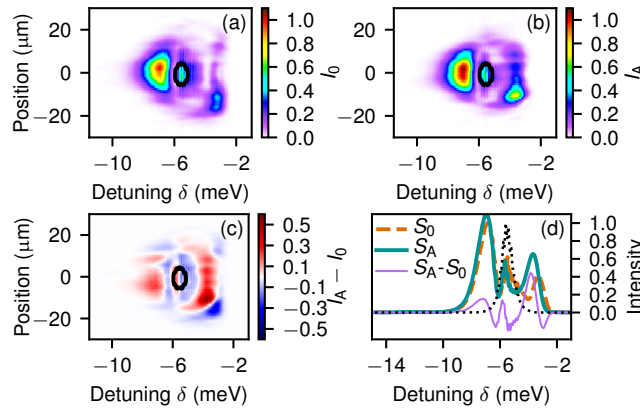


Fig. 3. Interplay of gain and nonlinear polariton-polariton interactions. (a) Output spectrum I_0 at zero pump and (b) amplified spectrum I_A at the highest pump power both for 7.2pJ probe pulse with central frequency detuning $\delta_0 = -5.6$ meV. The solid black curve denotes the half-maximum contour of the input pulse spectrum. (c) Difference between I_A and I_0 . The color scales are normalized to peak of I_0 . (d) Integrals S_0 and S_A of the spectra I_0 and I_A over the x direction, and the difference between S_0 and S_A , for pump and probe parameters corresponding to panels (a-c). The black dotted curve shows the spectrum of the input pulse.

We will now consider the effect of the gain on the nonlinear processes in the waveguide. Figure 3(a) shows the output spectrum $I_0(x, \delta)$ as a function of transverse position x and frequency relative to the exciton for the case of zero pump and an input pulse with energy 7.2 pJ and central frequency detuned by $\delta_0 = -5.6$ meV from the exciton line. At this power nonlinear self-phase-modulation (SPM) [33] occurs in both the transverse spatial (x) and temporal coordinates. The optical field accumulates an intensity-dependent phase as the pulse propagates which, through the pulse intensity profile, is a function of x and of time. This varying phase causes the spectrum to broaden. The black line in Fig. 3(a) shows the half-maximum contour of the spectrum of the pulse at the input. It can be seen that the spectrum of the pulse at the output, shown by the colour levels, is significantly broader.

When gain is applied the spectrum changes to $I_A(x, \delta)$ shown in Fig. 3(b) for the highest pump power. The difference between the I_A and the zero-pump spectrum I_0 is shown in Fig. 3(c). The integrals of these spectra over the spatial direction x are compared directly in Fig. 3(d). It can be seen that some spectral components are strongly amplified by up to 50% of the peak of I_0 while others are strongly de-amplified. Thus the shape of the spectrum is qualitatively modified by the presence of the gain. This arises from the combined effects of the gain, which modifies the

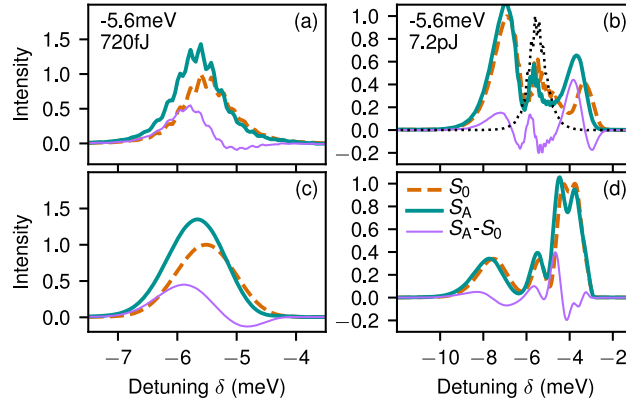


Fig. 4. Comparison of experimental and simulated spectra. All panels show the integrals S_0 and S_A of the unamplified and maximum-pump spectra I_0 and I_A over the x direction, and the difference between them, as identified in the legend in panel (d). (a) Experimental and (c) simulated spectra for 720fJ probe pulses. (b) Experimental and (d) simulated spectra for 7.2pJ probe pulses. The black dotted line in (b) gives the pulse spectrum at the waveguide input. All probe pulses have central frequency detuning $\delta_0 = -5.6$ meV.

intensity profile of the pulse, and the SPM, which gives an intensity dependent spectrum.

The effect of the gain on the nonlinear response is most dramatic for the highest energy probe pulses where the SPM is strong but it may also be seen for the 720 fJ pulses as shown in Fig. 4(a) for the $\delta_0 = -5.6$ meV detuning. Here we compare the spectra with zero pump and at the highest pump power. It can be seen that when the pump is strong, as well as being amplified, the pulse spectrum shifts to lower energies. The same spectral red-shift is observed for the other pulse detunings. The magnitudes of the spectral shifts obtained by fitting the lines with a sech² lineshape are 160 ± 20 μ eV, 150 ± 20 μ eV, and 80 ± 20 μ eV for detunings of -4.5 meV, -5.6 meV and -6.3 meV respectively. There was no significant change in spectral width. No shift was present for the 72fJ pulses where SPM is expected to be negligible. It is clear from Figs. 2(a) and 2(b) that the gain is lower for longer wavelengths (larger detuning from exciton) so the shift to longer wavelengths cannot be explained by preferential amplification of longer wavelength components but instead arises from the combination of gain and nonlinear response.

We now compare the experimental spectra to those obtained from the simulations. Figures 4(c) and 4(d) show simulated pulse spectra corresponding to the experimental ones in panels (a) and (b) respectively. The simulated spectra were obtained by numerically integrating Eq. (1) and Eq. (2) as described above. Comparing Figs. 4(b) and 4(d) the spectral broadening of the initially narrow pulse to produce S_0 (dashed orange line) is qualitatively reproduced by the simulation. Differences in the exact shape of the spectra between experiment and theory are probably due to the one-dimensional nature of the simulations (see Appendix A). These simulations therefore show that the spectral broadening indeed arises from the polariton interactions. When the gain is included in the simulation we can see by comparing S_0 (dashed orange) and S_A (solid green) in Fig. 4(d) that some spectral components are amplified and others attenuated, again showing qualitative agreement with the experiment. In both experiment and theory the maximum difference between amplified and unamplified spectra (thin lilac curve) is of order 40% of the peak of the unamplified spectrum. The change in spectrum with gain, which was seen in the experiment, is reproduced by the numerical model which confirms that it is due to the interplay of the gain and the interactions.

For the simulated spectra in Fig. 4(c), corresponding to 720 fJ pulse energy, the agreement with the experimental data in panel (a) is semi-quantitative, with both the size of the gain and the

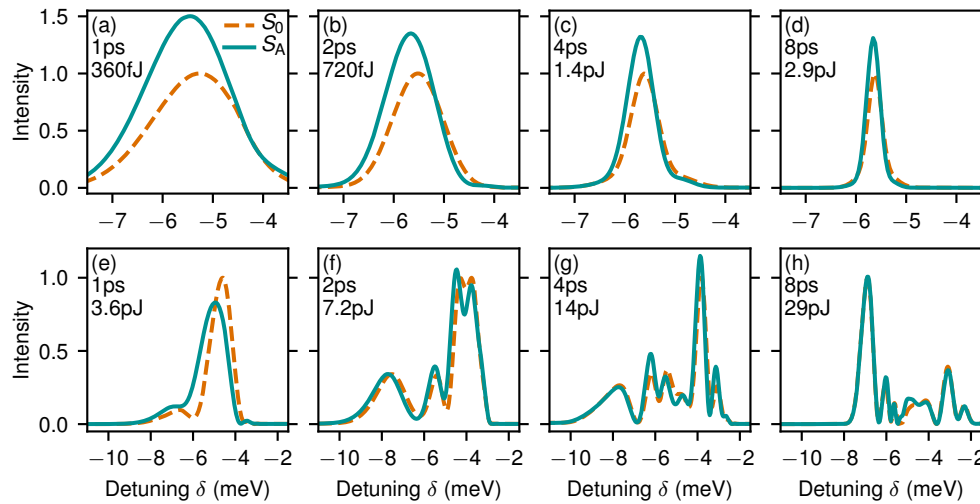


Fig. 5. Comparison of simulated output spectra for different input pulse temporal widths (full widths at half maximum). All panels show the spectrum without pump, S_0 , and the spectrum with maximum pump, S_A . The input pulse central frequency detuning for all pulses is $\delta_0 = -5.6$ meV. The peak density is fixed between pulses of different widths so the pulse energy varies proportional to the temporal width. (a-d) Spectra for pulses with the same peak density as the 2 picosecond, 720fJ pulse but temporal widths of 1, 2, 4 and 8 picoseconds respectively. (e-h) Spectra for pulses with the same peak density as the 2 picosecond, 7.2pJ pulse but temporal widths of 1, 2, 4 and 8 picoseconds respectively. In all panels the data are normalized to the peak of S_0 .

shift to longer wavelengths very closely reproduced. Overall these results show that we can fully understand the interplay of amplification and nonlinear effects in terms of the coupling of an incoherent reservoir and a coherent field of interacting lower-branch polaritons.

We finally consider the effect of pulse duration on the nonlinear response of the system and how it changes when the pulses are amplified. In Fig. 5 we show the simulated spectra at the output for pulses with several input temporal widths. When changing the temporal width the peak density is kept fixed so the total energy of the pulse varies proportionally to the pulse width. Fig. 5(a)–5(d) show results for pulses with the same peak density as the 2ps, 720fJ pulse considered earlier. As can be seen by comparing the peak heights of S_A between Fig. 5(a)–5(d), the gain is greater for the shorter pulses. This occurs because the shorter pulses contain less energy and so do not deplete the reservoir as much. It can also be seen that the amplification causes a spectral shift to lower frequency for all pulse lengths. The shift is larger for the shorter pulses, which may be explained because the amplification is larger for the shorter pulses.

We now consider the results for higher energy pulses shown in Fig. 5(e)–5(h). These all have the same peak density as the 2ps, 7.2pJ pulse considered earlier. Comparing S_0 for the different pulse lengths it can be seen that the spectral broadening and modulation caused by the nonlinearity is greater for the longer pulses and reduced for the shorter pulses. The peak input pulse density is the same between the different pulse lengths so in principle the nonlinear chirp developed should also be the same. However, as is well known from nonlinear fiber-optics [33], the effect of waveguide dispersion increases with the inverse square of the pulse length. This dispersion acts against the nonlinearity and thus reduces the modulation of the shorter pulses. For sufficiently short pulses the dispersion can even cancel the nonlinearity exactly, resulting in optical solitons [11]. Comparing the amplified spectra S_A to S_0 in Fig. 5(e)–5(h) it can be seen that the effect of the gain on the spectrum is greater for the shorter pulses, as was found for

the lower power pulses in Fig. 5(a)–5(d). These results show that the gain and its effect on the spectrum can be increased by using shorter pulses.

5. Conclusion

In conclusion, we have shown amplification of high velocity propagating picosecond polariton pulses with gain sufficient to overcome losses. We have shown that the gain is mainly limited by depletion of the reservoir. We observe combined gain and nonlinear modulation of the pulse spectra in the same device at the same time, with the pulse spectrum depending on the CW pump strength. This opens the door to new classes of pico-Joule pulse driven-dissipative nonlinear optical processing devices and photonic simulators in convenient sub-millimeter waveguides. Greater amplification could be provided at the same pump power level by using shorter pulses or by improving the overlap of the pulses with the gain, for example by confining the propagating polaritons and pumped region in the transverse direction using an etched ridge waveguide.

A. Details of numerical modelling

The parameters of Eq. (1) and Eq. (2) depend on the exciton and photon fraction making up the polariton and therefore depend on the pulse detuning which creates polaritons at a certain energy. The three pulse detunings $\hbar\omega_p = \delta_0 = -\{4.5, 5.6, 6.3\}$ meV correspond to a calculated exciton Hopfield fraction of $|X|^2 = \{0.500, 0.392, 0.336\}$ and a photon fraction $|C|^2 = 1 - |X|^2$. We then define effective parameter values [34] as: $\gamma = \gamma_e |X|^2 + \gamma_p |C|^2$ corresponding to exciton and photon lifetimes respectively, $\alpha = \alpha_0 |X|^4$, $g = 4\alpha_0 |X|^2$, and $R = R_0 |X|^2$. Fixed parameters of the model are taken from [12]: $\hbar\Omega = 9$ meV, $v_g = 58 \mu\text{m ps}^{-1}$, $\sigma_t = 0.85$ ps, $\sigma_z = 1.8 \mu\text{m}$, $z_0 = 120 \mu\text{m}$, $\sigma_{\text{CW}} = 47 \mu\text{m}$, $\gamma_p = 0.1 \text{ ps}^{-1}$, $\gamma_e = 0.04 \text{ ps}^{-1}$, $\Gamma = 0.1 \text{ ps}^{-1}$, $\alpha_0 = 3 \mu\text{eV } \mu\text{m}^2$, and $R_0 = 8 \mu\text{eV } \mu\text{m}^2$. We apply damped boundary conditions in both real space ($z < -50 \mu\text{m}$ and $z > 400 \mu\text{m}$) and reciprocal space ($|k| > 1 \mu\text{m}^{-1}$) to mimic respectively polaritons exiting the waveguide and higher losses for momenta far from resonance. Values of R_0 and Γ are chosen to fit experiment.

The simulations were performed in one dimension (z) and did not include the fact that the pulse envelope in the x direction is also free to evolve. This simplification is justified for the 72 fJ and 720 fJ pulses where nonlinear defocussing is weak but breaks down for the 7.2 pJ pulses. This likely explains why the exact shape of the broadened spectrum seen in Fig. 4(b) is not reproduced by the simulation shown in Fig. 4(d) even though the overall spectral broadening is correct. For the lower pulse energy shown in Fig. 4(a), where the 1D simplification is accurate, the simulation in Fig. 4(c) reproduces the experiment well.

B. Note on analysis of experimental data

As discussed in the main text the gain was measured by subtracting the spectrum S_{CW} due to the pump alone from the spectrum S_{tot} due to both pump and probe and comparing the result, S_A , to the spectrum S_0 due to the probe alone. Here we provide details of the signal-to-noise and signal-to-background ratios which are important for evaluating the reliability of this procedure. The main sources of random noise in the experiment are as follows: 1) Noise and dark counts in the CCD images which are present even when both lasers are off. 2) Fluctuations in the pulse energy, 3) Fluctuations in the CW laser power. The CCD dark counts are removed by subtracting a background image which is recorded with each data set for the case where both lasers are blocked. Comparing the background images from different data sets we find that, as expected, they are the same apart from fluctuations in the counts accumulated by each pixel which have a standard deviation of 13 counts. When integrating the CCD images to obtain total pulse intensity the sum was over at least 120 pixels so that the standard deviation in the integrated pulse intensity reduces to 1. Meanwhile the minimum number of integrated counts for a pulse was more than 2×10^5 so

that this source of noise is negligible. The fluctuations in probe pulse energy are easily found since a probe-only signal is recorded for every different CW power while the probe power is kept constant. Thus we need only to find the standard deviation of the integrated probe-only signal among these measurements. We find that the fluctuations are between 1% and 5% depending on the particular dataset. These fluctuations are taken into account in the error bars in Fig. 2. We deduce the fluctuations in CW laser power in a similar way by comparing the CW signal across repeated scans of the CW power. Thus for each CW power we have a set of nominally identical integrated intensities from which we can find the standard deviation. We find that the CW fluctuations are 1% of the integrated CW intensity. These fluctuations are also included in the error bars in Fig. 2. For propagating the uncertainties to obtain the uncertainty in the gain we assume that the fluctuations in the signal where both lasers are on is the sum of the fluctuations in the probe-only and pump-only signals. From an experimental point of view we minimised the effect of these fluctuations on the results by recording the spectra for pulse only, CW only, and with both lasers present within a short time interval of each other.

The signal-to-background ratio can be obtained by comparing the CCD image recorded with only the pulses present (CW pump laser off) to those recorded with only the CW laser on (probe laser off). To obtain the gain values plotted in Fig. 2 we integrated the images over a subset of CCD pixels corresponding to the spatial and spectral region close to the probe pulse signal. Considering this region the ratio of the peak probe pulse intensity to the peak CW intensity is always better than 0.8 for any combination of CW power and probe pulse power or detuning so that the signal and background are always at least comparable. After integration in the spatial direction the signal to background is always greater than 0.3. This can be seen directly in Fig. 1(b) where S_0 and S_{CW} are the signal (probe pulse) and background spectra respectively for the case of lowest probe power and highest pump power. The graph is normalised to the peak of S_0 so it can be seen that the background is 3 times higher than the signal. After also integrating with frequency δ the signal to background ratio is always greater than 0.6, at least 60 times larger than the fluctuations of 1% in the background intensity. We can therefore be confident in the reliability of our procedure of subtracting the data with only the CW laser one from that with both lasers on and then comparing the result to the data with only the pulse laser present. This is reflected in the size of the error bars compared to the data points in Fig. 2.

Since the probe pulse energy is low the average beam power is only only 5.8 micro-Watts at its minimum, about four orders of magnitude lower than the pump. However, as discussed, the signal is only a few times lower than the background. The reason that the signal-to-background ratio is much better than the ratio of probe and pump powers is that the background is generated by thermal relaxation of the zero-momentum excitons injected at the pump spot into the high-momentum and lower energy polariton states which are able to propagate towards the output grating. The exciton density of states is very large compared to that of the polaritons owing to the large exciton effective mass and inhomogeneously broadened distribution, a few meV wide [11]. Thus the polariton states which propagate from pump spot to output grating make up only a small fraction of the states available as end points for relaxation. Thus not much of the injected exciton density arrives at the output grating as background signal. By contrast the probe pulses propagate directly between the two gratings since they are deliberately injected with the correct frequency and momentum to match the guided mode.

C. Additional experimental details

The waveguide was grown by molecular beam epitaxy on a single-side-polished semi-insulating GaAs wafer. The layer sequence in order starting from the substrate is as follows: 500nm $\text{Al}_{0.9}\text{Ga}_{0.1}\text{As}$ which acts as a lower cladding, 25nm GaAs, three repeats of (10nm $\text{In}_{0.04}\text{Ga}_{0.96}\text{As}$ quantum well, 10nm GaAs barrier), 27nm GaAs, 3nm $\text{Al}_{0.9}\text{Ga}_{0.1}\text{As}$ etch stop layer, 20nm GaAs. The total thickness of the waveguide core region on top of the $\text{Al}_{0.9}\text{Ga}_{0.1}\text{As}$ cladding is 135nm.

The diffractive grating couplers were fabricated using electron-beam lithography and thermally evaporated metal in a lift-off process. The grating period was 250nm and within each period the gold stripes were 115nm wide. The metals used were, in order of deposition, 3nm of Titanium for adhesion to the GaAs followed by 20nm of Gold. After grating fabrication the sample was coated with a 345nm silicon nitride top cladding using plasma-enhanced chemical vapour deposition.

In previous measurements on the same waveguide [11, 12] the dispersion relation of the TE polarised uncoupled photon mode was found to have a group velocity of $58 \mu\text{m ps}^{-1}$ and to intercept the exciton resonance frequency at a propagation constant of $23.65 \mu\text{m}^{-1}$. Strong coupling between the TE mode and the exciton results in formation of upper and lower polariton states with a characteristic vacuum-Rabi-splitting of 9meV. Here we work exclusively with states on the lower polariton branch since the upper branch, above the exciton frequency, is very lossy. The anti-crossing of the photon and exciton results in a lower polariton mode with very large normal dispersion such that the dispersion of the uncoupled photons is negligible in comparison [11]. The TM polarised waveguide photon mode does not play a role in these measurements as it is close to cutoff, is strongly detuned, and does not form polaritons since the coupling of heavy-hole excitons to light polarised out of the quantum well plane is forbidden by selection rules.

The pump laser was a single-mode tuneable Ti:Sapphire laser. The probe pulses were produced by a tuneable modelocked Ti:Sapphire laser operating at a repetition rate of 80MHz. The spectral and temporal widths were measured at the output of the laser using, respectively, a commercial spectrometer and a commercial non-collinear second-harmonic-generation intensity autocorrelator. The spectral width was 0.66meV and the autocorrelation full-width-at-half-maximum (FWHM) of the pulses was 3.1ps corresponding to 2.0ps pulse intensity envelope for sech-squared pulses. The coupling of the pulses into the guided mode was optimised by monitoring the transmitted power at the output grating and tuning the incidence angle of the beam and the position of the spot relative to the edge of the input grating. The incidence angle was tuned independently from the position by translating the beam across the back focal plane of the objective. The grating coupling efficiency was estimated to be 15% using finite-difference-time-domain simulation.

The emission from the sample was collected using the same 20x magnification microscope objective as for excitation. The objective has effective focal length 10mm and numerical aperture of 0.6. A confocal 300mm lens formed an intermediate image plane at which an aperture was used to select only the emission from the vicinity of the output grating. The spatially filtered intermediate image plane was then transferred to the input slit of a Horiba Jobin Yvon TRIAX 320 imaging spectrometer using a pair of confocal lenses (500mm and 300mm) providing a total system zoom of 18x. The spectrometer has a focal length of 320mm and used a grating with 1200 lines per mm. The entrance slit width was set to 0.1mm. A Princeton Instruments PIXIS thermo-electrically cooled front-illuminated CCD array was fixed at the output plane of the spectrometer. The pixel size on the CCD array was $13 \mu\text{m} \times 13 \mu\text{m}$ and the array contains 1024×1024 pixels. The image of the sample was projected onto the entrance slit such that the edge of the output grating through which the light is coupled out (the edge parallel to x in the inset of Fig. 1(b)) coincided with the spectrometer slit and was parallel to it. Thus the camera simultaneously captures transverse position along one direction of the CCD array and wavelength along the other. The spectrometer resolution is $70 \mu\text{eV}$ at a wavelength of 837nm as measured using a single mode laser.

Funding

Engineering and Physical Sciences Research Council (EPSRC) (EP/J007544/1, EP/N031776/1); H2020 European Research Council (ERC) (Advanced Grant EXCIPOL 320570); CONACYT-Mexico doctoral scholarship programme; Leverhulme Trust (RPG-2013-339); Icelandic Centre

for Research (RANNIS) (163082-051); Ministry of Education and Science of the Russian Federation (Megagrant 14.Y26.31.0015, Goszadanie No. 3.2614.2017/4.6)

Acknowledgments

Data supporting this study are freely available from the University of Sheffield repository: <https://doi.org/10.15131/shef.data.7837322>.

References

1. I. Carusotto and C. Ciuti, "Quantum fluids of light," *Rev. Mod. Phys.* **85**, 299–366 (2013).
2. D. Sanvitto and S. Kéna-Cohen, "The road towards polaritonic devices," *Nat. Mater.* **15**, 1061–1073 (2016).
3. A. Amo, T. C. H. Liew, C. Adrados, R. Houdré, E. Giacobino, A. V. Kavokin, and A. Bramati, "Exciton-polariton spin switches," *Nat. Photonics* **4**, 361–366 (2010).
4. M. De Giorgi, D. Ballarini, E. Cancellieri, F. M. Marchetti, M. H. Szymanska, C. Tejedor, R. Cingolani, E. Giacobino, A. Bramati, G. Gigli, and D. Sanvitto, "Control and ultrafast dynamics of a two-fluid polariton switch," *Phys. Rev. Lett.* **109**, 266407 (2012).
5. A. Dreismann, H. Ohadi, Y. del Valle-Inclan Redondo, R. Balili, Y. G. Rubo, S. I. Tsintzos, G. Deligeorgis, Z. Hatzopoulos, P. G. Savvidis, and J. J. Baumberg, "A sub-femtojoule electrical spin-switch based on optically trapped polariton condensates," *Nat. Mater.* **15**, 1074–1078 (2016).
6. T. C. H. Liew, A. V. Kavokin, and I. A. Shelykh, "Optical circuits based on polariton neurons in semiconductor microcavities," *Phys. Rev. Lett.* **101**, 016402 (2008).
7. D. Ballarini, M. De Giorgi, E. Cancellieri, R. Houdré, E. Giacobino, R. Cingolani, A. Bramati, G. Gigli, and D. Sanvitto, "All-optical polariton transistor," *Nat. Commun.* **4**, 1778 (2013).
8. S. I. Tsintzos, N. T. Pelekanos, G. Konstantinidis, Z. Hatzopoulos, and P. G. Savvidis, "A GaAs polariton light-emitting diode operating near room temperature," *Nature* **453**, 372–375 (2008).
9. P. M. Walker, L. Tinkler, M. Durska, D. M. Whittaker, I. J. Luxmoore, B. Royall, D. N. Krizhanovskii, M. S. Skolnick, I. Farrer, and D. A. Ritchie, "Exciton polaritons in semiconductor waveguides," *Appl. Phys. Lett.* **102**, 012109 (2013).
10. P.-E. Larré and I. Carusotto, "Propagation of a quantum fluid of light in a cavityless nonlinear optical medium: General theory and response to quantum quenches," *Phys. Rev. A* **92**, 043802 (2015).
11. P. M. Walker, L. Tinkler, D. V. Skryabin, A. Yulin, B. Royall, I. Farrer, D. A. Ritchie, M. S. Skolnick, and D. N. Krizhanovskii, "Ultra-low-power hybrid light–matter solitons," *Nat. Commun.* **6**, 8317 (2015).
12. P. M. Walker, L. Tinkler, B. Royall, D. V. Skryabin, I. Farrer, D. A. Ritchie, M. S. Skolnick, and D. N. Krizhanovskii, "Dark solitons in high velocity waveguide polariton fluids," *Phys. Rev. Lett.* **119**, 097403 (2017).
13. P. G. Savvidis, J. J. Baumberg, R. M. Stevenson, M. S. Skolnick, D. M. Whittaker, and J. S. Roberts, "Angle-resonant stimulated polariton amplifier," *Phys. Rev. Lett.* **84**, 1547–1550 (2000).
14. R. Huang, F. Tassone, and Y. Yamamoto, "Experimental evidence of stimulated scattering of excitons into microcavity polaritons," *Phys. Rev. B* **61**, R7854–R7857 (2000).
15. G. Roumpos, C.-W. Lai, T. C. H. Liew, Y. G. Rubo, A. V. Kavokin, and Y. Yamamoto, "Signature of the microcavity exciton–polariton relaxation mechanism in the polarization of emitted light," *Phys. Rev. B* **79**, 195310 (2009).
16. R. M. Stevenson, V. N. Astratov, M. S. Skolnick, D. M. Whittaker, M. Emam-Ismael, A. I. Tartakovskii, P. G. Savvidis, J. J. Baumberg, and J. S. Roberts, "Continuous wave observation of massive polariton redistribution by stimulated scattering in semiconductor microcavities," *Phys. Rev. Lett.* **85**, 3680–3683 (2000).
17. J. J. Baumberg, P. G. Savvidis, R. M. Stevenson, A. I. Tartakovskii, M. S. Skolnick, D. M. Whittaker, and J. S. Roberts, "Parametric oscillation in a vertical microcavity: A polariton condensate or micro-optical parametric oscillation," *Phys. Rev. B* **62**, R16247–R16250 (2000).
18. H. Deng, H. Haug, and Y. Yamamoto, "Exciton-polariton bose-einstein condensation," *Rev. Mod. Phys.* **82**, 1489–1537 (2010).
19. D. Bajoni, P. Senellart, E. Wertz, I. Sagnes, A. Miard, A. Lemaître, and J. Bloch, "Polariton laser using single MicropillarGaAs-GaAlAsSemiconductor cavities," *Phys. Rev. Lett.* **100**, 047401 (2008).
20. R. Balili, V. Hartwell, D. Snoke, L. Pfeiffer, and K. West, "Bose-einstein condensation of microcavity polaritons in a trap," *Science* **316**, 1007–1010 (2007).
21. C. Schneider, A. Rahimi-Iman, N. Y. Kim, J. Fischer, I. G. Savenko, M. Amthor, M. Lermer, A. Wolf, L. Worschech, V. D. Kulakovskii, I. A. Shelykh, M. Kamp, S. Reitzenstein, A. Forchel, Y. Yamamoto, and S. Hoefling, "An electrically pumped polariton laser," *Nature* **497**, 348–352 (2013).
22. R. Houdré, J. L. Gibernon, P. Pellandini, R. P. Stanley, U. Oesterle, C. Weisbuch, J. O’Gorman, B. Roycroft, and M. Hegems, "Saturation of the strong-coupling regime in a semiconductor microcavity: Free-carrier bleaching of cavity polaritons," *Phys. Rev. B* **52**, 7810–7813 (1995).
23. G. Agrawal and N. Olsson, "Self-phase modulation and spectral broadening of optical pulses in semiconductor laser amplifiers," *IEEE J. Quantum Electron.* **25**, 2297–2306 (1989).
24. T. Saitoh and T. Mukai, "Recent progress in semiconductor laser amplifiers," *J. Light. Technol.* **6**, 1656–1664 (1988).
25. D. D. Solnyshkov, H. Tercas, and G. Malpuech, "Optical amplifier based on guided polaritons in GaN and ZnO," *Appl. Phys. Lett.* **105**, 231102 (2014).

26. O. Jamadi, F. Reveret, P. Disseix, F. Medard, J. Leymarie, A. Moreau, D. Solnyshkov, C. Deparis, M. Leroux, E. Cambriil, S. Bouchoule, J. Zuniga-Perez, and G. Malpuech, "Edge-emitting polariton laser and amplifier based on a ZnO waveguide," *Light. Sci. Appl.* **7**, 82 (2018).
27. S. V. Suchkov, A. A. Sukhorukov, J. Huang, S. V. Dmitriev, C. Lee, and Y. S. Kivshar, "Nonlinear switching and solitons in PT-symmetric photonic systems," *Laser Photonics Rev.* **10**, 177–213 (2016).
28. V. V. Konotop, J. Yang, and D. A. Zezyulin, "Nonlinear waves in PT-symmetric systems," *Rev. Mod. Phys.* **88**, 035002 (2016).
29. W. Chen, Ş. K. Özdemir, G. Zhao, J. Wiersig, and L. Yang, "Exceptional points enhance sensing in an optical microcavity," *Nature* **548**, 192–196 (2017).
30. S. Malzard, C. Poli, and H. Schomerus, "Topologically protected defect states in open photonic systems with non-hermitian charge-conjugation and parity-time symmetry," *Phys. Rev. Lett.* **115**, 200402 (2015).
31. M. Wouters and I. Carusotto, "Excitations in a nonequilibrium bose-einstein condensate of exciton polaritons," *Phys. Rev. Lett.* **99**, 140402 (2007).
32. K. Inoue, T. Mukai, and T. Saitoh, "Gain saturation dependence on signal wavelength in a travelling-wave semiconductor laser amplifier," *Electron. Lett.* **23**, 328 (1987).
33. G. P. Agrawal, *Nonlinear Fiber Optics* (Academic Press, 2001), 3rd ed.
34. A. S. Brichkin, S. I. Novikov, A. V. Larionov, V. D. Kulakovskii, M. M. Glazov, C. Schneider, S. Höfling, M. Kamp, and A. Forchel, "Effect of coulomb interaction on exciton-polariton condensates in GaAs pillar microcavities," *Phys. Rev. B* **84**, 195301 (2011).